Liao, S.; Gopalsami, N.; Elmer, T. W.; Koehl, E. R.; Heifetz, A.; Avers, K.; Dieckman, E.; Raptis, A. C.; , "Passive Millimeter-Wave Dual-Polarization Imagers," Instrumentation and Measurement, IEEE Transactions on , vol.61, no.7, pp.2042-2050, July 2012

DOI: 10.1109/TIM.2012.2183032

Passive Millimeter-Wave Dual-Polarization Imagers

S. Liao, N. Gopalsami*, T. W. Elmer, E. R. Koehl, A. Heifetz, K. Avers, E. Dieckman, and A. C. Raptis

***Abstract*—We have developed two passive millimeter-wave (mmW) imagers for terrestrial remote sensing: one is an integrated imaging and spectroscopy system in the 146-154 GHz range with 16 channels of 500 MHz bandwidth each and the other is a single channel dual polarized imaging radiometer in the 70-100 GHz range. The imaging in both systems is implemented through translation of a 15cm Gaussian dielectric imaging lens. We compared the outdoor images of objects like car, vegetation, sky, and ground by both the systems under various weather conditions including clear, cloudy and rainy times. Ray-tracing simulation with radiative transfer equation was used to quantify the polarization diversity of the acquired images.**

***Index Terms*—Millimeter-wave; radiometer; imaging; polarization**

I. Introduction

PASSIVE millimeter-wave (mmW) imaging has experienced dramatic growth in the past decade [1-8], due to its applications in terrestrial remote sensing, radiastronomy, and airport security. The main advantage of passive mmW imaging is that it can provide ground target information under all weather conditions; optical systems (visible and IR), on the other hand, require clear atmospheric conditions for reliable operation. For example, the atmospheric attenuation in the range of mmW frequencies is 0.07 to 3 dB/km in drizzle and fog conditions, whereas it is one to three orders of magnitude higher at optical frequencies (exceeding 100 dB/km in foggy conditions) [5],[6]. Image contrast of mm waves in outdoor environments is increased by cold sky-reflected radiation. For example, the apparent temperature of the sky at 94 GHz is 70K in comparison to 220K at infrared wavelengths. Because of reflectivity variations of common objects for millimeter waves (metal ~1, water 0.6, wood 0.6, and concrete 0.2), the mmW sky reflected radiation offers better thermal contrast than at infrared wavelengths. More important, signal "washouts" do not occur since the apparent temperature between the background and object will rarely be equal.

In addition, polarization diversity of passive mmW radiation may be used for enhanced discrimination of targets and surfaces. A common example is the change in apparent temperature of sea surface between horizontal and vertical polarizations depending on wind speed [4],[7],[8]. In this paper, we present results of horizontal and vertical polarization images from common ground targets such as car, ground, and trees. A ray tracing simulation is used to interpret the polarization diversity of the acquired images. We also present results of mmW imaging under various weather conditions at two frequency bands: a 16-channel radiometer in the 146 - 154 GHz range with 500 MHz bandwidth for each channel and a single-channel dual-polarization radiometer in the 70-100 GHz range.

The paper is organized as follows. The architectures of the two mmW radiometers are presented in Section II, followed by a description of the experimental imaging setup in Section III, and presentation of imaging results, analysis and discussion in Section IV, and conclusions in Section V.

II. mmW Radiometer Architectures

A. 16-channel 146 -154 GHz Radiometer

The architecture of our 16-channel radiometer [9] is shown in Fig. 1. It consists of a circular corrugated horn antenna, followed by a 146-154 GHz Band Pass Filter (BPF), a mixing stage, a 164 GHz Local Oscillator (LO) obtained by doubling an 82 GHz Gunn oscillator signal, an attenuator, a three-stage amplifier chain, and a 16-channel filter bank. A chopper is used in front of the scalar horn to collect Dicke-switched data between a reference signal from an absorber on the chopper blades and the target scene viewed through an opening between chopper blades. The detected signals from 16 channels are collected by a Data Acquisition (DAQ) board interfaced to a Laptop. To obtain 2-Dimensional (2D) images, a 15cm Gaussian lens was raster-scanned against the radiometer antenna positioned at the imaging plane of the lens. The use of 16 channels allows for detection of spectral signatures [10], while raster scanning a target for imaging.

Figure 2 gives, for example, results of imaging and spectroscopy conducted on a gas cell (7.5-cm ID, 8-cm OD, and 1 m long) containing acetonitrile (CH_3CN) vapor at different pressures, against a liquid nitrogen background. The solid portion of the gas cell has no spectral features but acetonitrile has rotational spectra in the 146-154 GHz range [11]. A 10x10 image was obtained across 15 spectral channels using 4s integration time per pixel. The scene was changed at the end of rows; the sequence of events consisted of (i) normalizing all 15 channels using cold (absorber immersed in

Manuscript received xx xx, 2011. This work is supported by the Office of Nonproliferation and Verification Research and Development under the National Nuclear Security Administration (NNSA) of the U.S. Department of Energy under Contract No. DE-AC02-06CH11357.

The authors are with the Argonne National Laboratory, Argonne, IL, 60439, USA.

*Corresponding author: Nachappa Gopalsami (phone: 630-252-5925; fax: 630-252-3250; e-mail: gopalsami@ anl.gov).

liquid nitrogen) and hot (absorber at ambient temperature) loads, (ii) vacuum (no gas) in the 1st row, (iii) pure CH_3CN at 2 Torr in rows 2-4, (iv) pure CH_3CN at 4 Torr in rows 5 and 6, (v) pure CH_3CN at 11 Torr in rows 7 and 8, (vi) air added to 11Torr CH_3CN to bring the total pressure to 740 Torr in row 9, and (vii) vacuum in row 10. The composite graph in Fig. 2 consists of individual images for 15 spectral channels at the top and spectral plots of acetonitrile at the bottom. The images of the channels are numbered 1 to 15 starting at the top row of images, which correspond to a center frequency of 146.75 GHz for Ch# 1 and increasing at 0.5 GHz interval to 153.75 GHz for Ch#15. The images show the circular part of the gas cell wall in all channels. Note that the molecular rotational spectrum of CH_3CN peaks around 146 GHz, so the image of CH_3CN is seen predominantly in the lower numbered channels depending on the extent of pressure broadening. The 11 Torr image is brighter than that of 4 Torr because of increased concentration and the 740 Torr image is weaker because of dilution with air and it is spread into more channels starting from Ch#1 because of pressure broadening. The spectral plots include simulated line at 4 Torr from JPL spectral data base [12] and the measured spectral plots at pressures 4, 11, and 740 Torr. The simulated and measured data at 4 Torr agree very well; the error bar is the standard deviation of intensity data from the pixels of same pressure. The pressure broadening effect is seen from the plots for 11 Torr and 740 Torr.

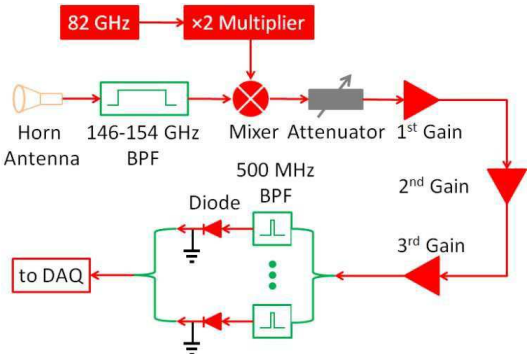

Fig. 1. Architecture of 16-channel 146-154 GHz radiometer with 500 MHz bandwidth for each channel.

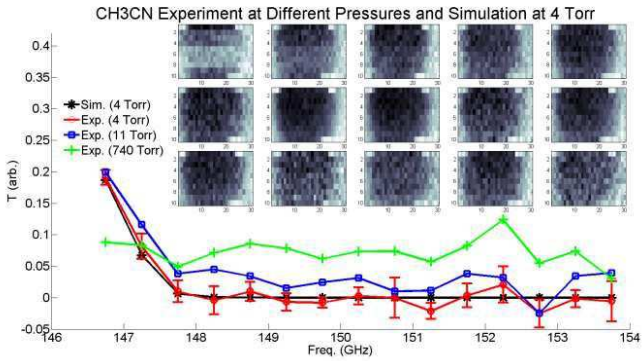

Fig. 2. Imaging and spectroscopy conducted on gas cell with acetonitrile at different pressures during image formation (vacuum at row 1, 2 Torr at rows 2-4, 4 Torr at rows 5-6, 11 Torr at rows 7-8, 740 Torr at row 9, and vacuum at row 10).

B. 70 –100 GHz Dual-polarization Radiometer

The architecture of our 70–100 GHz dual-polarization radiometer (Millitech MCA-10-100512) is shown in Fig. 3. It consists of a wire grid polarizer that splits the incoming signal into vertically and horizontally polarized signal paths. The signal in each path is received by a circular corrugated antenna and undergoes identical signal processing chain comprised of a 70–100 GHz BPF, a Low Noise Amplifier (LNA), a Schottky barrier diode detector and a baseband video amplifier. The baseband signals are collected by a DAQ interfaced to a Laptop. As in the 16-channel radiometer, a chopper may be used to collect Dicke-switched data, and the same 15cm Gaussian lens is raster scanned to obtain 2D images.

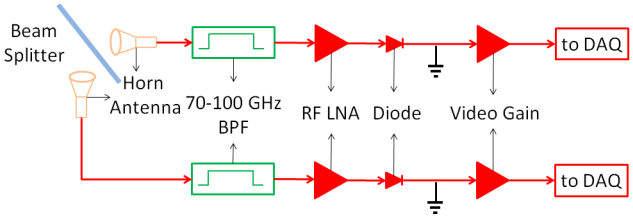

Fig. 3. Architecture of dual-polarization 70-100 GHz radiometer.

III. Experimental Setup

The experimental setup for our outdoor imaging is shown in Fig. 4. A LabVIEW® program running on a Laptop is used to collect and process the image data. The ray optics of the passive mmW imaging system was simulated by commercial software Zemax® to obtain optimal imaging parameters such as focal length and the distance between the horn antenna and the imaging lens, the details of which will be presented in the Discussion Section, together with determining the Point Spread Function (PSF) for both radiometers.

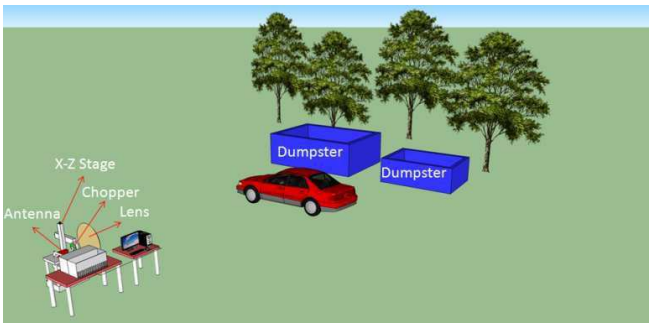

Fig. 4. Experimental setup for mmW imaging of outdoor scenes.

IV. Imaging Results, Analysis and Discussion

A. SNR Performance

For a Dicke-switched radiometer, the minimum detectable temperature, or Noise Equivalent Temperature Difference (NETD) is given by [13],

$$\mathrm{NETD} = (T_A + T_R)\sqrt{\left(\frac{1}{B\tau/2}\right)^2 + \left(\frac{\Delta G}{G}\right)^2} \sim 2(T_A + T_R)/\sqrt{B\tau} \quad (1)$$

where T_A and T_R are the antenna and the receiver temperatures, respectively; B is the bandwidth of the radiometer; $\tau/2$ is the integration time; and G and ΔG are the system gain and its variation. In Eq. (1), we have used the approximation $\Delta G/G \ll 1$, and the factor of 2 comes from the fact that a Dicke-switched radiometer only acquires signal at half the measurement time interval, τ. For our 16-channel 146 – 154 GHz radiometer [9, 10], $T_A = 290$ K; $T_R \sim 4492$ K; $B = 500$ MHz for each channel and if we assume the integration time $\tau = 1$ s, we have, NETD = 0.4 K; for our dual-polarization 70–100 GHz radiometer, $T_A = 290$ K; $T_R \sim 3000$ K; $B = 30$ GHz for each channel and if we assume the integration time $\tau = 1$ s, we get NEDT = 0.04 K. Obviously, the dual-polarization radiometer is more sensitive, due to two factors: larger bandwidth and the use of LNA at the frontend.

B. Radiative Transfer

The radiative signal from a solid object comes from two sources, the blackbody emission (Horizontal/Vertical polarization) of the object itself $I_o^{H/V}$ and the power reflection coefficient $R^{H/V}$ (defined as the square of the amplitude reflection coefficient) from the sky background emission $R^{H/V} I_b^{H/V}$. Both signals are subjected to the same absorption $e^{-\tau_o}$ from the object position z_o to the radiometer since they are along an identical path. The expression of the detected signal including atmospheric emission is given by [9],

$$I^{H/V} = \left(I_0^{H/V} + R^{H/V} I_b^{H/V}\right) e^{-\tau_o} + \int_0^{\infty} \kappa_a(z) T(z) e^{-\tau(z)} dz$$

$$\tau(z) = \int_0^{z} \kappa_a(z) dz\,, \quad \tau_o = \int_0^{z_o} \kappa_a(z) dz \qquad (2)$$

where κ_a is the absorption coefficient and $T(z)$ is the temperature along the wave path at altitude z. Rigorously all quantities in Eq. (2) depend on the frequency. However, in the frequency range of interest, the spectral changes are negligible for solid targets. The sky background emission may be slightly polarized, depending on the time of day and weather conditions (e.g., sunny, rainy, foggy etc.). But the most polarization contrast comes from the polarization dependent reflection $R^{H/V}$ since electromagnetic wave reflection from the interface between two dielectric materials is very different for horizontal and vertical polarizations. This can be easily understood by noting that there is no reflection for a vertically polarized wave at its Brewster angle of incidence, while there is no such magic angle for horizontal polarization [14]. So we would expect there will be polarization contrast when there is a reflection event involving a dielectric interface along the optical path of the imaging system, e.g., the reflection from the ground, the car windshield, the clouds in the sky, etc. In principle, the measured terrestrial image can be simulated using Eq. (2), with the help of ray-tracing method.

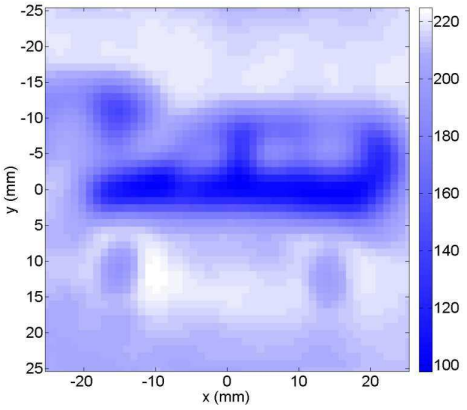

Fig. 5. Image of sum of all 16 channels of a 2001 white Mitsubishi Montero Sport car obtained by the 146 – 154 GHz radiometer (in K).

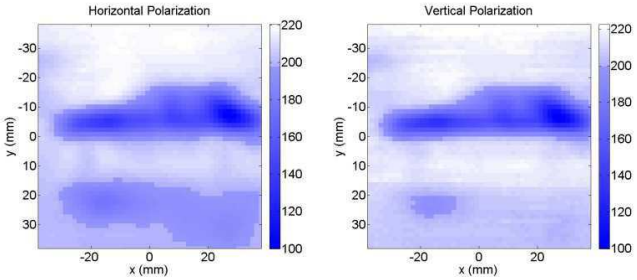

Fig. 6. Horizontal (left) and vertical (right) polarization images of a 2001 red Nissan Altima car obtained by the dual-polarization 70 – 100 GHz radiometer (in K).

C. Imaging Results and Analysis

The imaging scene, as shown in Fig. 4, typically consisted of a parked car at ~30 feet from the radiometer against the background of a dumpster(s), bushes, trees, and cold sky. We present imaging results of the above scene in both clear and rainy conditions and analyze the polarization contrast of the images.

1) *Clear and Cloudy Day Images:* Because of longer wavelength than of optics, mmW images of the scene during clear, cloudy, or day or night times showed no observable changes. Figure 5 shows the image of the scene with the 146–154 GHz radiometer with 2-second integration time (all channels summed up, which is equivalent to 8 GHz BW), and Fig. 6 shows the dual-polarization image with the 70 – 100 GHz radiometer with 1-second integration time taken on a fair weather day. The 146-154 GHz radiometer, being at a lower wavelength (2 mm), has a higher resolution than the (3 mm) 70–100 GHz radiometer. We can clearly see part of the dumpster, the car wheels and car windows from Fig. 5, while these are not so obvious in Fig. 6. However, due to narrower bandwidth of the 16-channel radiometer (8 GHz compared to 30 GHz of the dual-polarization radiometer), it takes about twice the integration time to obtain similar SNR.

Typical acquisition time for a 50 x 50 image with 1s integration time is approximately 1 h. This is typical of scanned single pixel imaging systems, but one may employ compressive sensing to speed up the imaging time by a factor of ten or more [15]. The advantage of single pixel imaging compared to video rate imaging using an array of detectors is that it offers high SNR and allows for the use of one-of-a-kind

sophisticated detectors such as the 146-154 GHz imaging and spectroscopy system we have built.

The polarization changes in the images may be analyzed using the ray tracing method. Figure 7 classifies the image scene into five regions for ray tracing analysis: #1, the image of the trees behind the car, which consists of the tree emission and the reflection of sky background emission by the tree, #2, reflection of sky background emission by the upper part of the car's front side; #3, reflection of sky background emission by the ground and then by the lower part of the car's front side; #4, reflection of sky background emission by the upper part of the car's front side and then by the ground; and #5, reflection of the trees by the ground.

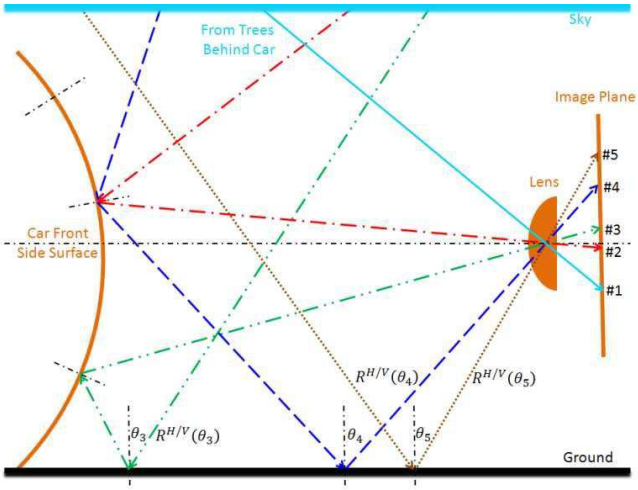

Fig. 7. Image scene analysis using ray-tracing method.

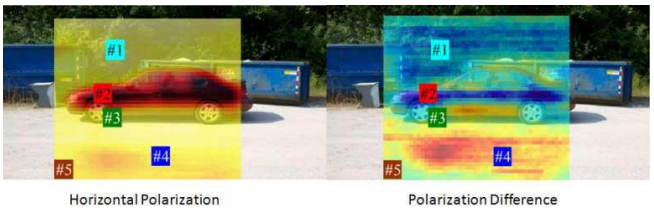

Fig. 8. Horizontal-polarization image (left) and polarization difference image (right) overlaid on the optical images of the car. The horizontal-polarization image is the same as in Fig. 6 with a different color map and the polarization difference image is the subtraction of the vertical-polarization image from the horizontal-polarization image of Fig. 6 Also shown are 5 different regions that correspond to those analyzed in Fig. 7.

Figure 8 shows (a) the horizontal polarization image overlaid on the optical image of the car and (b) the polarization difference image. The corresponding five regions of Fig. 7 are marked in Fig. 8 (a) and (b). The trees behind the car (region #1) emit unpolarized radiation at outdoor temperature, which is much higher than the reflection of the sky background emission. Hence, we can consider that the trees image has almost the same intensity for both polarizations. Because the car front surface (region #2) is made of metal, its emission is almost zero and its reflection of sky background emission is not sensitive to polarization. The sky radiation reflected by the ground and bottom part of the car (region #3) show small changes in polarization because of small incidence angles. On the other hand, the sky reflection from the ground (region #4) causes strong polarization contrast because of different reflection coefficients for vertical and horizontal polarizations at such large incidence angles. The ground reflected radiation of trees (region #5) offers less polarization contrast due to smaller temperature contrast.

From the geometry of the scene, we can simulate the scene image and compare it to the measured image. We calculate the reflections for both polarizations from the measurement data and compare them to theoretical calculation. Figure 9 shows the measured reflections for both polarizations, which are calculated for the car reflection by the ground according to Eq. (2), ignoring the relatively small absorption coefficient κ_a ,

$$R^{H/V} = I^{H/V}(\#4) - I_{Ground} \Big/ I^{H/V}(\#2) \qquad (3)$$

where I_{Ground} is the ground emission. We can clearly see the contour of the car and detailed features such as the car windows with the help of nonlinear operation of Eq. (3), while

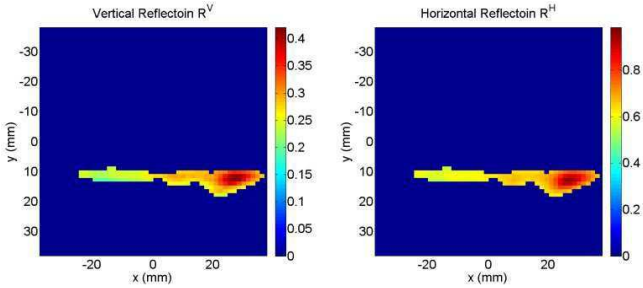

Fig. 9. Measured reflection power coefficients of both vertical (left) and horizontal (right) polarizations.

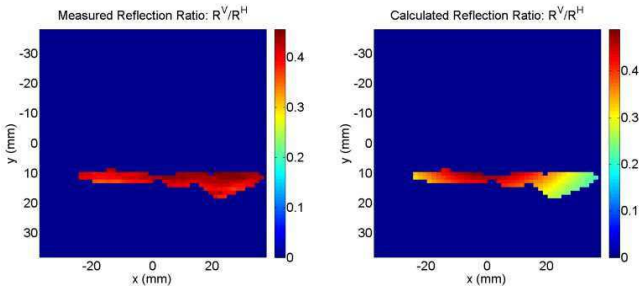

Fig. 10. Ratio of vertical power reflection coefficient to horizontal power reflection coefficient $ratio \equiv R^V / R^H$: on the left are the measured values and on the right are the simulated values.

they were not so obvious in the raw images of Fig. 6. Also, Fig. 10 shows the ratio of vertical reflection to horizontal reflection $ratio \equiv R^V / R^H$ and its comparison to the theoretical value [14]. For theoretical calculation, we have used the dry ground permittivity $\varepsilon_{Ground} = 3.5$ and the distance from the antenna to the Gaussian lens $d_i = 7.5''$. The incident angle of region #4 in Fig. 6 is given by

$$\theta_i(\#4) = \arctan\left[\sqrt{x^2(\#4) + y^2(\#4)} \Big/ d_i\right] \qquad (4)$$

Now the horizontal and vertical reflection coefficients can be obtained as [14]:

$$R^H(\#4)=\left|\eta_2\cos\theta_i-\eta_1\cos\theta_t \Big/ \eta_2\cos\theta_i+\eta_1\cos\theta_t\right|^2$$

$$R^V(\#4)=\left|\eta_2\cos\theta_t-\eta_1\cos\theta_i \Big/ \eta_2\cos\theta_t+\eta_1\cos\theta_i\right|^2$$

$$\sin(\theta_t)=\gamma_{Air}\Big/\gamma_{Ground}\sin(\theta_i)\ ,\quad \gamma\equiv j\omega\sqrt{\mu_0\varepsilon_0(\varepsilon'-j\varepsilon'')} \quad (5)$$

where η_1 and η_2 are wave impedances of air and ground respectively. Also, the Brewster angle of the ground is $\theta_B=\arctan\left[\sqrt{\varepsilon_{Ground}}\right]\sim 62^\circ$ for the vertical polarization, which is smaller than the incident angle $\theta_i(\#4)\sim 80^\circ$, as calculated from Eq. (4). Note that only the metallic part of the car is shown in Figs. 9 and 10 since non-metallic dielectric materials like car windows behave differently, i.e., instead of completely reflecting all polarizations, dielectric materials reflect polarized wave differently and is thus polarization sensitive.

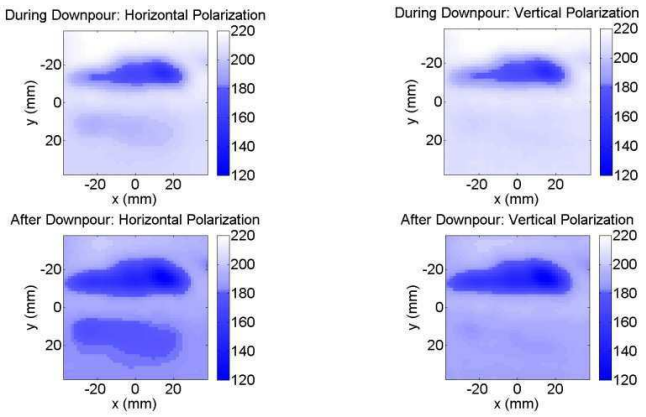

Fig. 11. Dual-polarization images during rainfall (top) and after rainfall (bottom) show different polarization contrast for the 2001 Nissan Altima car used in Fig. 6.

2) *Rainy Day Images*: The top and bottom images in Fig. 11 give the dual-polarization images during moderate rain and after the rain stopped, respectively. Clearly the temperatures of the trees and ground are higher during rainfall. This is because the millimeter-wave emission of rain droplets is much higher than that of the sky. Also in Fig. 11, we give the images of the power reflection ratio between vertical polarization and horizontal polarization according to Eq. (3). One can see that the polarization contrast is higher during rainfall (which is $R^V/R^H\sim 0.35$) compared to that after rain stopped (which is $R^V/R^H\sim 0.2$). This is because the rain changes the dielectric constant of the ground and thus the power reflection according to Eq. (5).

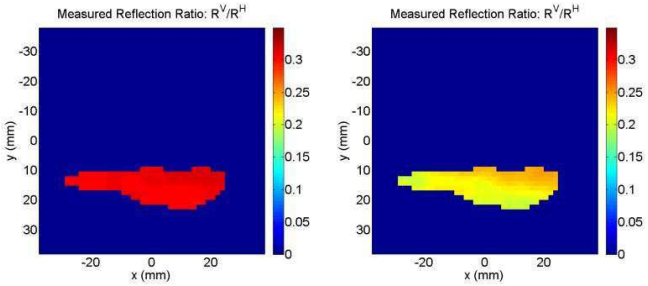

Fig. 12. Power reflection ratio between vertical polarization and horizontal polarization: during rainfall (left) and after rainfall (right).

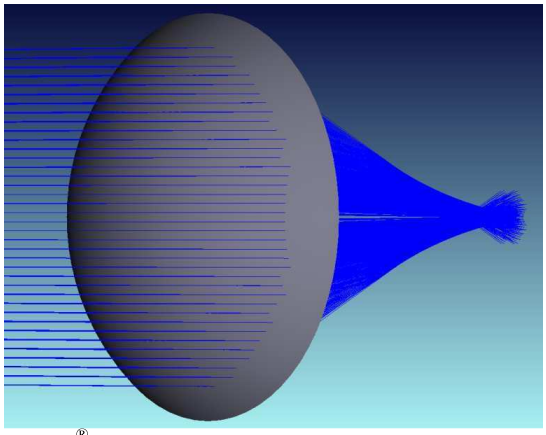

Fig. 13. Zemax® simulation of 15-cm imaging lens shows the focal length, the optical depth and the PSF at 100 GHz.

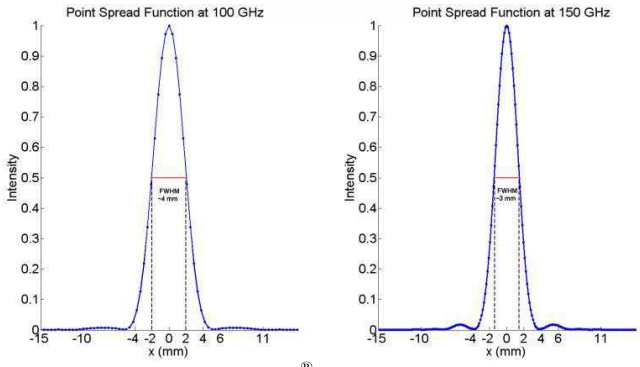

Fig. 14. Simulated PSF using Zemax® at 100 GHz (the dual-polarization radiometer) and 150 GHz (the 16-channel radiometer).

V. Discussion

From the images obtained with both radiometers, it is clear that the 146–154 GHz radiometer provides higher resolution than that of the dual-polarization 70–100 GHz radiometer because of its shorter wavelength. This may be quantitatively verified using the ray tracing software Zemax®. Figure 13 shows the ray tracing simulation of a 15cm lens at 100 GHz. The focal length determined from the simulation is: $f\sim 16.5$ cm at 100 GHz and $f\sim 16.76$ cm at 150 GHz. The distance from the detecting antenna to the imaging lens, d_i, follows the standard imaging formula $1/f=1/d_i+1/d_o$, with d_o being the distance from the imaging lens to the scene. Since the

resolution of an image is the convolution of the scene with the PSF, we can obtain the PSFs for both cases. Figure 14 shows the optical transfer function (OTF) obtained at 100 GHz (or 3 mm wavelength) for the dual-polarization radiometer and at 150 GHz (or 2 mm wavelength) for the 16-channel radiometer. The Full Width at Half Maximum (FWHM) for the two frequencies are: FWHM ~ 4 mm at 100 GHz and FWHM ~ 3 mm at 150 GHz. The PSF is closely related to the Optical Transfer Function (OTF); the PSF and the Modulation Transfer Function (MTF) which is the magnitude of the OTF, are a Fourier transform pair, $PSF = IFT\{MFT\} = IFT\{|OTF|\}$ [16]. The knowledge of the PSF for the imagers will be useful in the image analysis and recognition of targets in cluttered environment.

VI. Conclusions

We have developed two radiometers for terrestrial imaging and spectroscopic application, the 16-channel 146–154 GHz radiometer and the dual-polarization 70–100 GHz radiometer. Zemax® optics software was used to optimize the passive mmW imaging optics and to determine the PSF of the imagers. Images of an outdoor scene consisting of a car, dumpsters, trees, and the sky were taken under different weather conditions to compare their performance. It has been shown that the 16-channel radiometer has higher resolution due to its shorter wavelength. However, its SNR is lower than that of the dual-polarization radiometer due to the narrower bandwidth, so longer integration time is required to obtain images of the same quality. The polarization contrast is mainly due to reflection from the interface of two dielectric materials such as the ground, the car windshield, and the clouds in the atmosphere. The polarization changes from the vertical and horizontal reflections of the sky radiation by the car and the ground were analyzed using a combination of ray tracing and radiative transfer simulation. The shadow of the car by the ground which was not obvious in the raw image became evident with the above analysis. We also extended the analysis to determine the polarization changes of the scene under rainy conditions. These results show that ray-tracing method in combination the radiative transfer equations is a powerful tool for scene simulation and image analysis for passive mmW systems.

References

[1] M. A. Janssen, Ed., *Atmospheric* Remote Sensing by Microwave Radiometry, New York: Wiley, 1993.

[2] J. J. Lynch, P. A. Macdonald, H. P. Moyer, and R. G. Nagele, "Passive millimeter wave imaging sensors for commercial markets," Applied Optics, Vol. 49, No. 19, 2010.

[3] M. R. Fetterman, J. Grata, J. G. Jubic, W. L. Kiser, Jr, and A. Visnansky, "Simulation, acquisition, and analysis of passive millimeter-wave images in remote sensing applications," Optics Express, 16, 20503-20515, 2008.

[4] M. Peichl, S. Dill, M. Jirousek, J. W. Anthony and H. Sub, "Fully-polarimetric passive mmW imaging systems for security applications," Proc. SPIE 7837, 78370C, 2010.

[5] L. Yujiri, M. Shoucri, and P. Moffa, "Passive millimeter-wave imaging," IEEE Microwave Magazine, September, 2003.

[6] R. Appleby and R. N. Anderson, "Millimeter-wave and submillimeter-wave imaging for security and surveillance," Proc. IEEE, 95, 1683-1690, 2007.

[7] N. Skou and D. M. Le Vine, Microwave Radiometer Systems: Design and Analysis, Norw*ood, MA: Ar*tech House, 2006.

[8] C. W. O'Dell, D. S. Swetz, and P. T. Timbie, "Calibration of Millimeter wave polarimeters using a thin dielectric sheet," IEEE Trans. on Microwave Theory and Techniques, vol. 50, pp. 2135-2141, 2002.

[9] N. Gopalsami, S. Bakhtiari, T. W. Elmer, A. C. Raptis, "Application of millimeter-wave radiometry for remote chemical detection," IEEE Transactions on Microwave Theory and Techniques, Vol. 56, No. 3, March, 2008.

[10] N. Gopalsami, S. Liao, E. R. Koehl, T. W. Elmer, A. Heifetz, H. T. Chien and A. C. Raptis, "Passive millimeter wave imaging spectroscopy system for terrestrial remote sensing," Proceedings of SPIE, Vol. 7670, pp. 767003-1:767003-7, 2010.

[11] N. Gopalsami and A. C. Raptis, "Millimeter-wave radar sensing of airborne chemicals," IEEE Trans. on Microwave Theory and Techniques, vol. 49, pp. 646-653, 2001.

[12] R. L. Poynter and H. M. Picket, Submillimeter, Millimeter, and Microwave Spectral Line Catalog. Pasadena, CA: Jet Propulsion Lab., vol. 80-23, 1983.

[13] M. Sato, T. Hirose and K. Mizuno, "Advanced MMIC receiver for 94-GHz band passive millimeter-wave imager," IEICE Trans. on Electron., Vol. E92. C, No. 9, pp. 1124-1129, 2009.

[14] C. A. Balanis, *Advanced Engineering Electromagnetics*, John Wiley & Sons, Inc., 1998.

[15] N. Gopalsami, T. W. Elmer, S. Liao, R. Ahern, A. Heifetz, A. C. Raptis, M. Luessi, D. Babacan and A. K. Katsaggelos, "Compressive sampling in passive millimeter-wave imaging," Proceedings of SPIE, Vol. 8022, pp. 802201-1: 802201-6, 2011.

[16] J. W. Goodman, Introduction to Fourier Optics, the McGraw-Hill : New York, 1996.

Shaolin Liao received the B.S. degree in materials science and engineering from Tsinghua University, Beijing, China, in July 2000, the M.S. degree in material science and the M.S. degree in electrical and computer engineering, both from the University of Wisconsin at Madison, in August 2003 and December 2005, respectively, and the Ph.D. degree in electrical and computer engineering from the University of Wisconsin at Madison, in May 2008. Dr. Liao held the research fellow position in Physics department, Queens College, City University of New York from May 2008 to January 2010. He is now with Argonne National Laboratory, doing microwave/millimeter wave/THz wave/laser research.

Dr. Liao has been interested in both active and passive millimeter wave applications like remote sensing, Non-Destructive Examination (NDE) and national security, both experiment and theory; high-power microwave transmission and conversion; gyrotron component design; microwave beam shaping technique; theory and algorithm development for high-performance simulation of electromagnetic wave propagation and scattering; antenna design and simulation; as well as microwave and light multiple scattering and Anderson localization inside random media.

Nachappa ``Sami" Gopalsami received his B.E. and M.S. degrees in Electrical Engineering from the University of Madras, India and Ph.D. degree in Electrical Engineering and Computer Science from the University of Illinois, Chicago. He joined Argonne National Laboratory in 1980 where he is currently a senior electrical engineer in the Sensors and Instrumentation section of the Nuclear Engineering Division. His current research interests include development of radio frequency, microwave, millimeter-wave, and terahertz sensors and imaging systems for national security, biosensing, environmental monitoring, and materials applications. Dr. Gopalsami has published over 150 technical papers in the area of sensors and NDE and has seven U.S. patents to his credit. He has received two R&D 100 awards from the R&D Magazine, both on millimeter wave sensors in 1986 and 2007; an outstanding paper award from the American Society of Nondestructive Testing; and an Outstanding Mentor award from the Office of Science Undergraduate Research Programs. He is a senior member of IEEE and a member of Sigma Xi and SPIE.

Thomas Elmer II received the B.S. degree in physics with minors in math and computer science from La Sierra University in 1998 and the M.S. degree in Physics from the University of Illinois, Chicago in 2004. While at La Sierra, he worked for the physics department, writing and maintaining programs to run laboratory experiments. He has also lectured on Astronomy and Gravitational Physics for the department. In 1999 he joined Argonne National Laboratory as a student intern, eventually staying as a Software Engineering Associate for the System Technologies & Diagnostics Department of the Nuclear Engineering Division. He writes programming for modeling, motion control, data acquisition, and data analysis in the microwave, millimeter-wave, and terahertz sensors labs. In 2007 he received an R&D 100 award from R&D Magazine.

Eugene R. Koehl received a B.A. in Physics from Lewis University in 1969 and a B.S. in Electrical Engineering from Midwest College of Engineering (Illinois Institute of Technology) in 1981. He is an electrical engineer at Argonne National Laboratory with 37 years of experience in the design, fabrication, instrumentation, control, and automated data acquisition of experiments and facilities for testing the design and characteristics of sensors, power systems and LMR components. His activities cover a broad range of physical sciences including acoustic signal transport, x-ray inspection and detection, high and process vacuum, alkali metal chemistry and heat transport, satellite tracking and millimeter wave systems. He has been involved with the precision manipulation and non-destructive testing of engineered materials used in heavy vehicle, stationary power, and aerospace systems for the past 16 years.

Alexander Heifetz is an Electrical Engineer with Nuclear Engineering Division at Argonne National Laboratory. Alex came to Argonne as Director's Postdoctoral Fellow with Nuclear Engineering Division. His research interests are in simulations and modeling for electromagnetic engineering, nuclear engineering, signal processing and controls. He received a Ph.D. in Electrical Engineering, M.S. in Physics and B.S. (Summa Cum Laude) in Applied Mathematics, all from Northwestern University. Alex has published over 20 peer-reviewed papers in major scientific journals, and has one provisional US Patent.

Keenan Avers is an undergraduate student at the University of Illinois at Chicago (UIC), currently working on his BA in engineering physics. He joined Argonne National Laboratory as a student intern in the summer of 2010 and again in the summer of 2011. He assisted the Millimeter Wave group in assembling and operating the 70-100 GHz dual polarization radiometer. He is currently working for the Nanoscale Physics group in the UIC physics department where he assists in preparation of thin film oxide samples.

Eric Dieckman is an undergraduate student at Purdue University majoring in physics. He joined Argonne National Laboratory in the summer of 2011as a student intern, where he worked on the Zemax simulation software for millimeter wave optics.

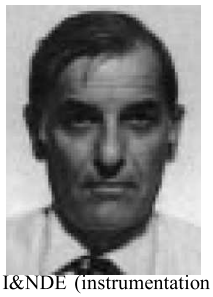

Apostolos C. Raptis is a senior electrical engineer at Argonne National Laboratory with 35 years of experience in teaching and in research and development. His areas of expertise include sensors, instrumentation and controls, nondestructive evaluation, data processing, electromagnetics, plasmas, optics, acoustics and geophysical exploration. He is presently the department manager for Systems Technologies and Diagnostics in the Nuclear Engineering Division. At ANL he initiated and helped develop ANL's I&NDE (instrumentation and NDE) programs for nuclear and fossil energy, conservation and arms controls. He is responsible for work on national security for remote detection of chemical, biological, nuclear agents and explosives. In addition, he has been a strong participant in collaborative work with the University of Chicago in the development of the Bioengineering initiative. He is the author of more than 250 publications and holder of 17 patents, as well as the recipient of the 1994, 1996, 2007, and 2011 R&D 100 awards, and 1994 ASNT best paper award.

List of Figure Captions

Fig. 1. Architecture of 16-channel 146-154 GHz radiometer with 500 MHz bandwidth for each channel.

Fig. 2. Imaging and spectroscopy of gas cell with acetonitrile at different pressures during image formation (vacuum at row 1, 2 Torr at rows 2-4, 4 Torr at rows 5-6, 11 Torr at rows 7-8, 740 Torr at row 9, and vacuum at row 10).

Fig. 3. Architecture of dual-polarization 70-100 GHz radiometer.

Fig. 4. Experimental setup for mmW imaging of outdoor scenes.

Fig. 5. Image of sum of all 16 channels of a 2001 white Mitsubishi Montero Sport car obtained by the 146 – 154 GHz radiometer (in K).

Fig. 6. Horizontal (left) and vertical (right) polarization images of a 2001 red Nissan Altima car obtained by the dual-polarization 70 – 100 GHz radiometer (in K).

Fig. 7. Image scene analysis using ray-tracing method.

Fig. 8. Horizontal-polarization image (left) and polarization difference image (right) overlaid on the optical images of the car. The horizontal-polarization image is the same as in Fig. 6 with a different color map and the polarization difference image is the subtraction of the vertical-polarization image from the horizontal-polarization image of Fig. 6. Also shown are 5 different regions that correspond to those analyzed in Fig. 7.

Fig. 9. Measured reflection power coefficients of both vertical (left) and horizontal (right) polarizations.

Fig. 10. Ratio of vertical power reflection coefficient to horizontal power reflection coefficient $ratio \equiv R^V / R^H$: on the left are the measured values and on the right are the simulated values.

Fig. 11. Dual-polarization images during rainfall (top) and after rainfall (bottom) show different polarization contrast for the 2001 Nissan Altima car used in Fig. 6.

Fig. 12. Power reflection ratio between vertical polarization and horizontal polarization: during rainfall (left) and after rainfall (right).

Fig. 13. Zemax® simulation of 15-cm imaging lens shows the focal length, the optical depth and the PSF at 100 GHz.

Fig. 14. Simulated PSF using Zemax® at 100 GHz (the dual-polarization radiometer) and 150 GHz (the 16-channel radiometer).